

# Phase transitions and gluodynamics in 2-colour matter at high density

Tamer Boz<sup>1</sup>, Seamus Cotter<sup>1</sup>, Leonard Fister<sup>1</sup>, Dhagash Mehta<sup>2</sup>, and Jon-Ivar Skullerud<sup>1</sup>

<sup>1</sup> Department of Mathematical Physics, National University of Ireland Maynooth, Maynooth, County Kildare, Ireland

<sup>2</sup> Department of Physics, Syracuse University, Syracuse, NY 13244, USA

Received: date / Revised version: date

**Abstract.** We investigate 2-colour QCD with 2 flavours of Wilson fermion at nonzero temperature  $T$  and quark chemical potential  $\mu$ . From temperature scans at fixed  $\mu$  we find that the critical temperature for the superfluid to normal transition depends only very weakly on  $\mu$  above the onset chemical potential, while the deconfinement crossover temperature is clearly decreasing with  $\mu$ . We find indications of a region of superfluid but deconfined matter at high  $\mu$  and intermediate  $T$ . The static quark potential determined from the Wilson loop is found to exhibit a ‘string tension’ that increases at large  $\mu$  in the ‘deconfined’ region. The electric (longitudinal) gluon propagator in Landau gauge becomes strongly screened with increasing temperature and chemical potential. The magnetic (transverse) gluon shows little sensitivity to temperature, and exhibits a mild enhancement at intermediate  $\mu$  before becoming suppressed at large  $\mu$ .

**PACS.** 11.15Ha Lattice gauge theory – 12.38Aw Lattice QCD calculations – 21.65Qr Quark matter – 12.38Mh Quark-gluon plasma

## 1 Introduction

The properties and phase diagram of quantum chromodynamics (QCD) at large baryon density remain largely unknown, despite substantial theoretical efforts. One important reason for this is the failure of traditional Monte Carlo methods for lattice QCD at nonzero density, due to the infamous sign problem. While progress has been made in the region of high temperature  $T$  and moderate baryon chemical potential  $\mu_B$ , the region of low  $T$  and large  $\mu_B$  remains inaccessible to Monte Carlo simulations.<sup>1</sup>

There are, however, QCD-like theories which are not affected by the sign problem, at least for an even number of flavours  $N_f$ , among them QCD with gauge groups  $SU(2)$  (QC<sub>2</sub>D) [5, 6, 7], or  $G_2$  [8], with nonzero isospin density [9] or with adjoint fermions [10]. These theories allow first-principles lattice simulations and may hence be used as benchmarks for other methods that are not encumbered by the sign problem, but which may involve uncontrolled approximations. Such methods may include model studies such as NJL and quark-meson models (possibly augmented by a Polyakov loop potential); effective theories valid for example for heavy quarks or at high density; or functional methods such as the functional renormalisation group (FRG), Dyson–Schwinger equations (DSEs)

or  $n$ -particle irreducible (nPI) methods, which rely on assumptions about higher-order vertices.

Among these QCD-like theories, QC<sub>2</sub>D is the simplest, both mathematically and computationally, and hence provides the greatest scope for quantitative tests of other approaches. It has already been used to test analytic continuation methods at high temperature and low density [11, 12] and to compare model studies with lattice results (see [13, 14, 15] for some recent examples).

In a recent paper [7] the first steps were taken towards mapping out the phase diagram of QC<sub>2</sub>D in the  $(\mu, T)$  plane, by identifying at least 3 distinct regions characterised by vanishing or nonvanishing diquark condensate  $\langle qq \rangle$  and Polyakov loop  $\langle L \rangle$ :

- a vacuum or hadronic phase at low  $T$  and  $\mu$ , characterised by vanishing quark number density  $n_q$  and with  $\langle qq \rangle = 0$ ,  $\langle L \rangle \approx 0$ ;
- a superfluid, confined (quarkyonic) region at low  $T$  and intermediate to large  $\mu$ , with  $\langle L \rangle \approx 0$ ,  $\langle qq \rangle \neq 0$ ;
- a deconfined quark–gluon plasma at high  $T$ , with  $\langle L \rangle \neq 0$ ,  $\langle qq \rangle = 0$ ; and possibly
- a deconfined, superfluid region at large  $\mu$  and intermediate  $T$ , with  $\langle L \rangle \neq 0$ ,  $\langle qq \rangle \neq 0$ .

Rough estimates were presented for the phase boundaries between these regions. In the present paper, we study the phase boundaries in more detail and attempt to pinpoint their location.

We will also attempt to cast further light on the confining properties of the theory at low temperature and the

<sup>1</sup> Some progress has recently been made using complex Langevin [1, 2] and other methods [3, 4], but neither have as yet been shown to work for QCD.

nature of the putative deconfinement transition at high density, by computing the static quark potential in the low-temperature region.

In contrast to quantities which may not be directly comparable between theories, the effects of the medium on low order Green functions in QC<sub>2</sub>D may provide a reliable guideline to full QCD. Quark and gluon correlation functions are of great interest, as the theory can be fully expressed in terms of these. Propagators play a predominant role, in particular in continuum descriptions, and in some cases their behaviour suffices to shed light on the critical physics of the phase diagram, e.g. the deconfinement transition [16, 17, 18, 19]. In this paper, we will study how the gluon propagator responds to both temperature and quark chemical potential.

In Sec. 2 we set out the details of our lattice simulations, including the action, parameters and lattice volumes used. Then, in Sec. 3 we study the superfluid to normal and deconfinement transition by performing a temperature scan at 3 different values of the chemical potential. The response of the static quark potential to  $\mu$  is investigated in Sec. 4, while in Sec. 5 results for the gluon propagator are reported. Preliminary results for the gluon propagator have been reported in [20, 21], and for the static quark potential in [22].

## 2 Simulation details

We use a standard Wilson gauge action with two flavours of unimproved Wilson fermion, with the addition of a diquark source term to lift the low-lying eigenmodes and allow a controlled study of diquark condensation effects. Further details about the action and the simulation method can be found in [5, 6, 7]. The results obtained will depend on the diquark source  $j$ ; in the end the  $j \rightarrow 0$  limit must be taken to obtain ‘physical’ results.<sup>2</sup>

We use the same parameters as in [6, 7], namely  $\beta = 1.9, \kappa = 0.168$ , corresponding to a lattice spacing  $a = 0.178(6)\text{fm}$  and a pion mass  $am_\pi = 0.645(8)$ . The lightest baryon, the scalar diquark, is degenerate with the pion in the vacuum, and at zero temperature we therefore expect an onset transition to a superfluid phase at  $m = m_\pi/2$ . This has been corroborated in previous simulations [5, 6, 7].

In addition to the ensembles used and described in [7], we have generated gauge configurations on  $16^3 \times N_\tau$  lattices with  $N_\tau = 4-20$ , in order to study in detail the thermal transitions at  $a\mu = 0.35, 0.4, 0.5$  and  $0.6$ . The details of these ensembles are given in table 1. For most temperatures, two diquark sources  $ja = 0.02$  and  $0.04$  have been used, enabling us to perform a linear extrapolation to the  $j = 0$  limit. In the region of the superfluid to normal transition, where a linear extrapolation is known to be in-

<sup>2</sup> In cases where model studies could be carried out with  $j \neq 0$  one might also compare directly results for nonzero  $j$ ; however, most other studies will not contain any explicit diquark source term, so the  $j \rightarrow 0$  limit is crucial.

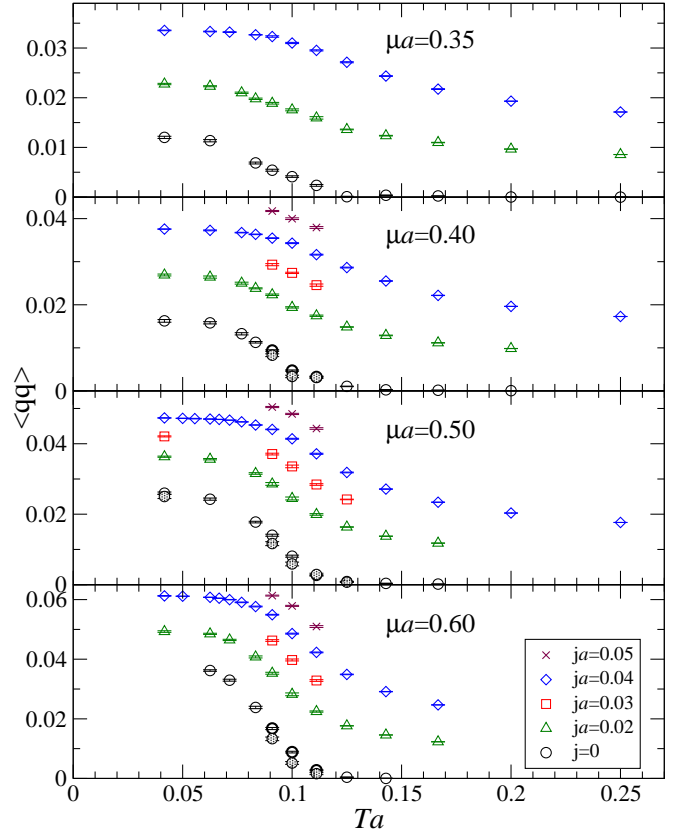


**Fig. 1.** Diquark condensate  $\langle qq \rangle$  as a function of temperature  $T$  for chemical potential  $\mu a = 0.35, 0.4, 0.5, 0.6$  (top to bottom). The circles are data extrapolated to  $j = 0$  using a linear Ansatz for  $ja \leq 0.04$ ; the shaded circles denote the results of a linear extrapolation using  $j = 0.02, 0.03$  only.

valid, two additional  $j$ -values have been added to allow for a controlled extrapolation.

## 3 Phase transitions

### 3.1 Superfluid to normal transition

Figure 1 shows the order parameter for superfluidity, the diquark condensate

$$\langle qq \rangle = \langle \psi^{2tr} C \gamma_5 \tau_2 \psi^1 - \bar{\psi}^1 C \gamma_5 \tau_2 \bar{\psi}^{2tr} \rangle, \quad (1)$$

as a function of the temperature  $T$ , for  $\mu a = 0.35, 0.4, 0.5$  and  $0.6$ . Also shown are the results of a linear extrapolation to  $j = 0$ . We can clearly observe a transition from a superfluid phase, characterised by  $\langle qq \rangle \neq 0$ , at low temperature, to a normal phase with  $\langle qq \rangle = 0$  at high temperature, with a transition in the region  $0.08 \lesssim Ta \lesssim 0.12$  for all three values of  $\mu$ . In order to pinpoint the transition, we have performed simulations with 4 different  $j$ -values in the transition region, and used 3 different functional

$\mu a$	$ja$	$N_\tau$														
		20	18	16	15	14	13	12	11	10	9	8	7	6	5	4
0.35	0.02			270			370	250	270	510	560	800	520	1100	300	250
0.35	0.04			250		270		4550	710	500	500	675	510	900	300	250
0.4	0.02			270			250	500	500	500	550	1000	250	250	300	
0.4	0.03								250	280	300					
0.4	0.04						1020	1080	1050	1000	1000	1050	1000	1000	1000	1000
0.4	0.05								250	240	216					
0.5	0.02			280				512	250	255	275	1000	250	300		
0.5	0.03								280	270	280	1000				
0.5	0.04	3075	3020	2570	3835	3340	3200	3240	2620	1000	1000	1050	1200	1000	1200	1000
0.5	0.05								300	270	270					
0.6	0.02			350		320		310	300	300	300	1000	300	300		
0.6	0.03								290	280	280					
0.6	0.04	4200		2300	2210	1840	1000	1128	1005	1000	1040	1200	1020	1000		
0.6	0.05								255	300	300					

**Table 1.** Number of trajectories for different temperatures,  $T = 1/(aN_\tau)$ , chemical potentials  $\mu$  and diquark sources  $j$ . All trajectories have average length 0.5, and the spatial lattice size is  $N_s = 16$  in all cases.

forms for the  $j \rightarrow 0$  extrapolation,

$$\text{linear:} \quad \langle qq \rangle = A + Bj, \quad (2)$$

$$\text{power law:} \quad \langle qq \rangle = Bj^\alpha, \quad (3)$$

$$\text{constant + power:} \quad \langle qq \rangle = A + Bj^\alpha. \quad (4)$$

The results of these extrapolations are summarised in table 2. We find that the linear form is clearly disfavoured; however, the pure power law does not give a good fit either in most cases, while the constant + power Ansatz is unstable and tends to give a negative intercept at  $j = 0$ . Clearly, more work is needed to obtain good control over the  $j \rightarrow 0$  extrapolation.

With our current data at only a single volume we are not in a position to determine the order of the transition, although it would be expected to be a second order phase transition in the universality class of the 3-dimensional XY model. This could be tested by attempting a universal fit of the data at  $j \neq 0$  in the transition region to a scaling form given by the appropriate critical exponents: note that at fixed  $\mu$ , the diquark source  $j$  would be the magnetic field variable in this scaling function. This would also provide an alternative method for determining  $T_s$ .

Because of the uncertainties in the  $j \rightarrow 0$  extrapolation in the critical region, we have estimated the critical temperatures  $T_s$  for the superfluid to normal transition by determining the inflection points for  $\langle qq \rangle$  at  $ja = 0.02$  and  $0.04$ , and extrapolated the resulting values to  $j = 0$  using a linear Ansatz. The results are given in table 3. We see that  $T_s$  is remarkably constant over the whole range of  $\mu$ -values considered. The indications are that the transition happens at a somewhat lower temperature at  $\mu a = 0.35$ , but this point is already very close to the onset from vacuum to superfluid at  $T = 0$ ,  $\mu_o a = m_\pi a/2 = 0.32$ , suggesting that  $T_s(\mu)$  rises very rapidly from zero at  $\mu = \mu_o$  before suddenly flattening off.

Fit	$\mu a$	$N_\tau$	$A$	$B$	$\alpha$	$\chi^2/N_{df}$
(2)	0.4	9	0.0036(1)	0.695(3)		26
	0.4	10	0.0056(1)	0.711(4)		102
	0.4	11	0.0096(1)	0.646(4)		9.8
	0.5	9	0.0037(2)	0.829(4)		51
	0.5	10	0.0095(2)	0.790(6)		54
	0.5	11	0.0155(2)	0.712(6)		45
	0.6	9	0.0034(2)	0.966(4)		46
	0.6	10	0.0095(2)	0.976(6)		48
	0.6	11	0.0203(2)	0.849(6)		180
(3)	0.4	9		0.490(8)	0.852(5)	7.4
	0.4	10		0.438(7)	0.793(5)	40
	0.4	11		0.321(5)	0.683(5)	11
	0.5	9		0.617(10)	0.875(5)	28
	0.5	10		0.439(9)	0.734(6)	9.4
	0.5	11		0.315(6)	0.612(6)	1.6
	0.6	9		0.746(11)	0.893(5)	20
	0.6	10		0.576(9)	0.767(5)	19
	0.6	11		0.357(6)	0.584(5)	55
(4)	0.4	9	-0.003(1)	0.76(4)	0.40(3)	8.7
	0.4	10	-0.019(4)	0.47(4)	0.24(1)	3.2
	0.4	11	0.003(3)	0.85(6)	0.45(4)	*
	0.5	9	-0.008(2)	0.70(4)	0.42(3)	29
	0.5	10	-0.012(4)	0.55(5)	0.31(3)	*
	0.5	11	-0.005(4)	0.54(5)	0.28(2)	0.88
	0.6	9	-0.010(2)	0.69(3)	0.48(3)	0.05
	0.6	10	-0.006(4)	0.68(6)	0.59(6)	*
	0.6	11	-0.055(12)	0.28(4)	0.269(4)	*

**Table 2.** Parameters for the  $j \rightarrow 0$  extrapolation of  $\langle qq \rangle$  in the transition region, using a linear (2), power-law (3) and power + constant (4) Ansatz. All four values of  $j$  have been used. Where there is a star in the column for  $\chi^2/N_{df}$ , the central fit value was outside the 68% confidence interval, and the quoted value is instead taken to be in the middle of the 68% confidence interval.

$a\mu$	0.35	0.40	0.50	0.60
$aT_s(0.04)$	0.121(6)	0.108(2)	0.111(5)	0.102(6)
$aT_s(0.02)$	0.097(16)	0.096(5)	0.097(2)	0.093(5)
$aT_s$	0.073(24)	0.084(8)	0.083(5)	0.083(6)
$T_s$ (MeV)	82(27)	94(9)	93(6)	93(7)

**Table 3.** Inflection points  $T_s(j)$  for  $\langle qq \rangle(T)$  at  $ja = 0.04, 0.02$  and critical temperature  $T_s$  obtained from extrapolating  $T_s(j)$  to  $j = 0$ . The uncertainties are estimates of the systematic uncertainty in determining the inflection points and in the  $j \rightarrow 0$  extrapolation.

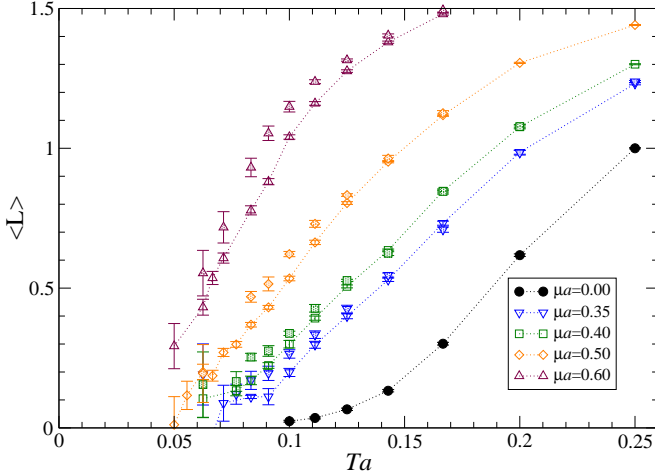


**Fig. 2.** The renormalised Polyakov loop  $\langle L \rangle$  as a function of temperature  $T$  for  $\mu a = 0.35, 0.4, 0.5$  and  $0.6$ , in addition to the  $\mu = j = 0$  results from [7]. The open symbols are results for  $ja = 0.04$ ; the shaded symbols are for  $ja = 0.02$ .

### 3.2 Deconfinement transition

Figure 2 shows the traditional order parameter for deconfinement, the Polyakov loop  $\langle L \rangle$ , as a function of temperature for different values of  $\mu$ . The Polyakov loop has been renormalised using the same method as described in [7, 23], by imposing the condition that  $L(aT = \frac{1}{4}, \mu = 0) = 1$ . This determines the renormalisation constant  $Z_L$  in the relation between the bare Polyakov loop  $L_0$  and the renormalised Polyakov loop  $L_R$ ,

$$L_R(T, \mu) = Z_L^{N_\tau} L_0\left(\frac{1}{aN_\tau}, \mu\right). \quad (5)$$

At all  $\mu$ , we see a transition from a low-temperature confined region to a high-temperature deconfined region. In contrast to the diquark condensate, we see a clear, systematic shift in the transition region towards lower temperatures as the chemical potential increases.

For all four  $\mu$ -values, the Polyakov loop shows a nearly linear rise as a function of temperature in a broad region, suggesting that the transition is a smooth crossover rather than a true phase transition. For this reason, it is difficult if not impossible with our present data to identify an inflection point which we could use as a definition of a pseudocritical deconfinement temperature. We choose instead to define the crossover region as the region where

$\mu a$	$T_d a$	$T_d$ (MeV)
0.0	0.193(20)	217(23)
0.35	0.101–0.179	113–200
0.40	0.087–0.157	97–176
0.50	0.057–0.103	64–115
0.60	0.050–0.097	56–109

**Table 4.** Estimates for the deconfinement crossover temperature  $T_d$  from the Polyakov loop at  $ja = 0.04$ . The  $\mu = 0$  result is taken from [7].

the Polyakov loop at  $ja = 0.04$  rises approximately linearly with  $T$ . From Fig. 2 we see that the value of  $\langle L \rangle$  increases as  $j$  is reduced, and at  $\mu a = 0.6$  at least, the crossover region will most likely move to smaller  $T$  in the  $j \rightarrow 0$  limit. However, we do not have sufficient statistics for  $ja = 0.02$  at low  $T$  to make any quantitative statement about this.

In the low-temperature region, an accurate determination of the renormalised Polyakov loop becomes increasingly difficult because of the exponential growth of the renormalisation factor  $Z_L^{N_\tau}$ . Extending the data in fig. 2 to  $Ta < 0.05$  ( $N_\tau > 20$ ) is beyond our present capabilities.

Our summary of transition temperatures taken from the  $ja = 0.04$  data is given in table 4.

## 4 Static quark potential

The potential between two static quarks (or a quark–antiquark pair), and in particular its asymptotic behaviour at large separations, has traditionally been taken as the tell-tale indicator, or even definition, of confinement of quarks [24]. A linearly rising potential has been observed in numerous lattice simulations, and has also formed the basis of successful phenomenological descriptions of bound states of heavy quarks. In QCD with dynamical quarks, the string will break at a finite distance, but at intermediate distances a linear rise can still be observed.

At high temperature, the potential is expected to exhibit Debye screening, and this has been observed in numerous calculations of the quark–antiquark free energy using Polyakov loop correlators. However, it is not yet clear how this quantity relates to the (complex) potential that appears in effective theories of heavy quarkonia at high temperature [25, 26, 27, 28]. Very recently, the static quark potential has also been determined from Wilson loops at high temperature [29]; this does not show any screening for  $T \lesssim T_c$ .

There has also been some recent progress in determining the potential between heavy (finite mass) quarks at zero [30] and non-zero [31] temperature. Some properties of bound states of heavy quarks in QC<sub>2</sub>D at nonzero temperature and density were reported in [32]; a potential model description should reproduce these results. Here we compute the static quark potential from Wilson loops for our lowest temperature, the  $12^3 \times 24$  lattices.

In fig. 3 we show the static quark potential computed from the Wilson loop at  $N_\tau = 24$ , for  $\mu a = 0.3, 0.5, 0.7, 0.9$

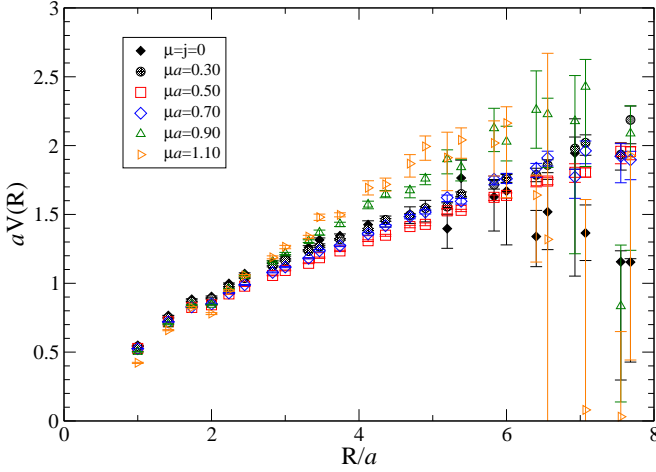


**Fig. 3.** The static quark potential computed from the Wilson loop, for the  $12^3 \times 24$  lattice and different values of  $\mu$ , with  $ja = 0.04$ .

and 1.1. We find that as we enter the superfluid region, the potential becomes slightly flatter, but that this is reversed as  $\mu$  is increased further, leading to a strongly enhanced string tension at  $\mu a = 0.9$ , which according to our analysis of the Polyakov loop should be in the deconfined region. This agrees with the pattern that was already observed in [5].

To quantify the variation of the static quark potential with  $\mu$ , we have performed a fit to the Cornell potential,

$$V(r) = C(\mu, j) + \sigma(\mu, j)r + \frac{\alpha(\mu, j)}{r}, \quad (6)$$

for each  $\mu$  and  $j$ . The results for the “string tension”  $\sigma$  and the Coulomb factor  $\alpha$  are shown in fig. 4. For  $\mu a < 0.6$  we do not see any systematic trend, but for larger  $\mu$  we find that  $\sigma$  increases rapidly and roughly linearly with  $\mu$ , accompanied by a similar decrease in  $\alpha$ . We also see that there is no significant dependence on the diquark source  $j$ .

The lack of screening at large  $\mu$  is consistent with what was observed at high  $T$  in [29]. At present we do however not have a good understanding of why the static quark potential should become antiscreened at large  $\mu$ . There are several possibilities:

1. The transition may be to a medium characterised by long-range interactions, rather than by colour screening. If that is the case, one would expect typical correlation lengths to also grow with  $\mu$ . Reconciling a linearly rising potential with a nonzero Polyakov loop remains a challenge, however.
2. The quark–antiquark potential is screened at large distances, but this is not observed in the Wilson loop because of poor overlap with the relevant states. This corresponds to the standard scenario at low temperature, where explicit mesonic states must be introduced to observe string breaking [33]. Clearly, our observation of a linearly rising potential (area law for the Wilson loop) does not prove that the medium is confining.

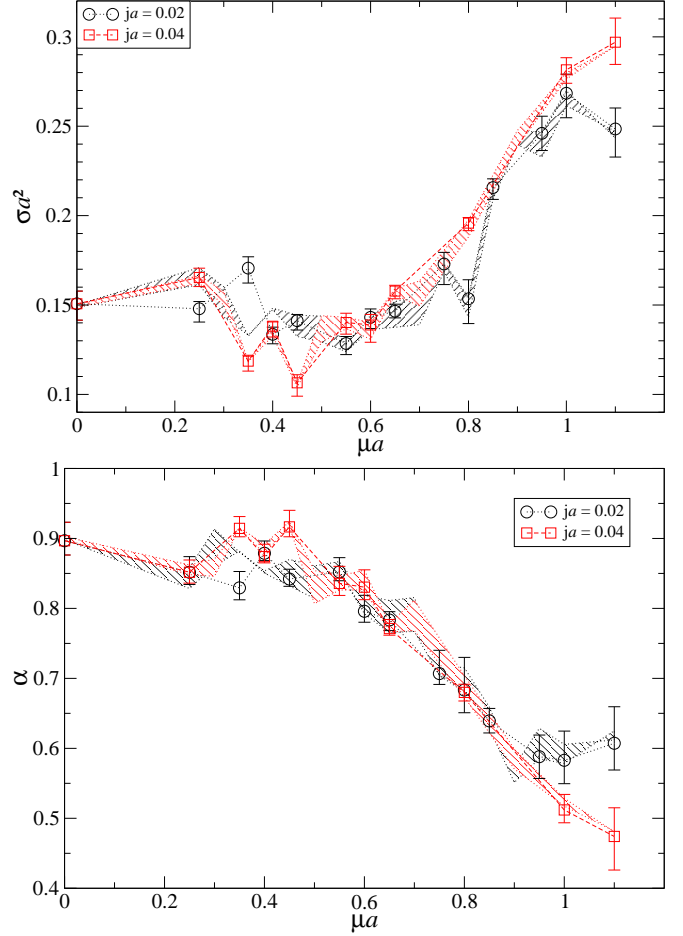


**Fig. 4.** The parameters  $\sigma$  (top) and  $\alpha$  (bottom) in the Cornell potential (6), as a function of the chemical potential  $\mu$ , for the  $12^3 \times 24$  lattice. The error bars are statistical uncertainties, while the bands indicate systematic uncertainties estimated from varying the fitting range in  $R$ .

The increasing slope could however be indicative of a large internal energy for static quark–antiquark pairs at intermediate distances.

- In [32] it was found that the binding energy of heavy quarkonia in QC<sub>2</sub>D increases up to  $\mu a \approx 0.7$ , and decreases again beyond that. This appears to run counter to the conjecture above, in which the quarkonium might be expected to become more strongly bound.
3. A more pessimistic scenario is that the whole region of  $\mu a > 0.6$  could be dominated by lattice artefacts. Unfortunately our previous data at  $\beta = 1.7$  [5] are probably outside the scaling region so a comparison with those is likely to be not very revealing. Simulations at smaller  $a$ , which are underway, should confirm or rule out this scenario.

Computing the static quark potential using Polyakov loop correlators rather than Wilson loops might yield further insight into this issue. However, the Polyakov loop correlator suffers from the same signal to noise problem at low  $T$  (large  $N_\tau$ ) as the Polyakov loop itself, and we have not been able to obtain any signal for  $N_\tau = 24$  ex-

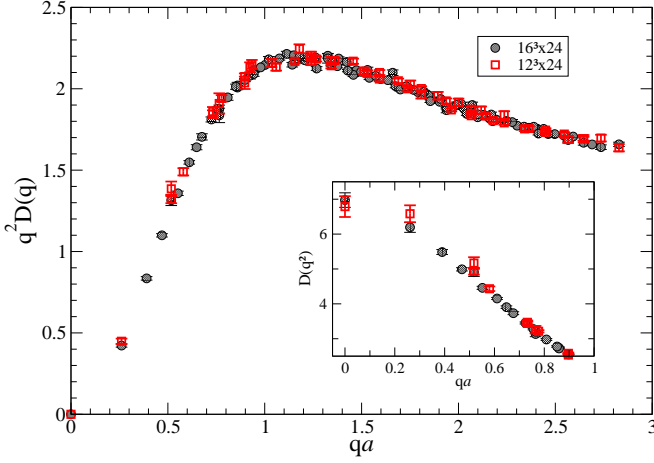


**Fig. 5.** The gluon dressing function in the vacuum from the  $16^3 \times 24$  and  $12^3 \times 24$  lattice. The inset shows the gluon propagator for infrared momenta. A cylinder cut has been applied to the data to reduce lattice spacing artefacts.

cept for  $\mu a \gtrsim 0.9$ . Results for higher temperatures using both the Wilson loop and Polyakov loop correlators will be presented in a future publication.

## 5 Gluon propagator

In this section we extend previous studies [5, 20, 21] and present results for in-medium gluon propagators, where we study the dependence on both parameters, chemical potential and temperature. In Landau gauge only the transverse part of the vacuum propagator is non-zero. However, the external parameters break manifest Lorentz invariance, hence the gluon propagator  $D$  must be decomposed into chromoelectric and chromomagnetic modes,  $D_E$  and  $D_M$ , respectively,

$$D_{\mu\nu} = P_{\mu\nu}^M D_M + P_{\mu\nu}^E D_E, \quad (7)$$

where the individual dependence on (discrete) temporal and spatial momenta has been omitted. The projectors on the longitudinal and transversal spatial subspaces,  $P_{\mu\nu}^E$  and  $P_{\mu\nu}^M$ , are defined by

$$\begin{aligned} P_{\mu\nu}^M(q_0, \mathbf{q}) &= (1 - \delta_{0\mu})(1 - \delta_{0\nu}) \left( \delta_{\mu\nu} - \frac{q_\mu q_\nu}{\mathbf{q}^2} \right), \\ P_{\mu\nu}^E(q_0, \mathbf{q}) &= \left( \delta_{\mu\nu} - \frac{q_\mu q_\nu}{\mathbf{q}^2} \right) - P_{\mu\nu}^M(q_0, \mathbf{q}). \end{aligned} \quad (8)$$

We have fixed our gauge configurations to Landau gauge by maximising the gauge fixing functional

$$F[U, g] = \sum_{x, \mu} \text{Tr} U_\mu^g(x) = \sum_{x, \mu} \text{Tr} g(x) U_\mu(x) g^\dagger(x + \hat{\mu}), \quad (9)$$

using the standard overrelaxation algorithm. The Landau gauge condition has been imposed with a precision  $|\partial_\mu A_\mu| < 10^{-10}$ .

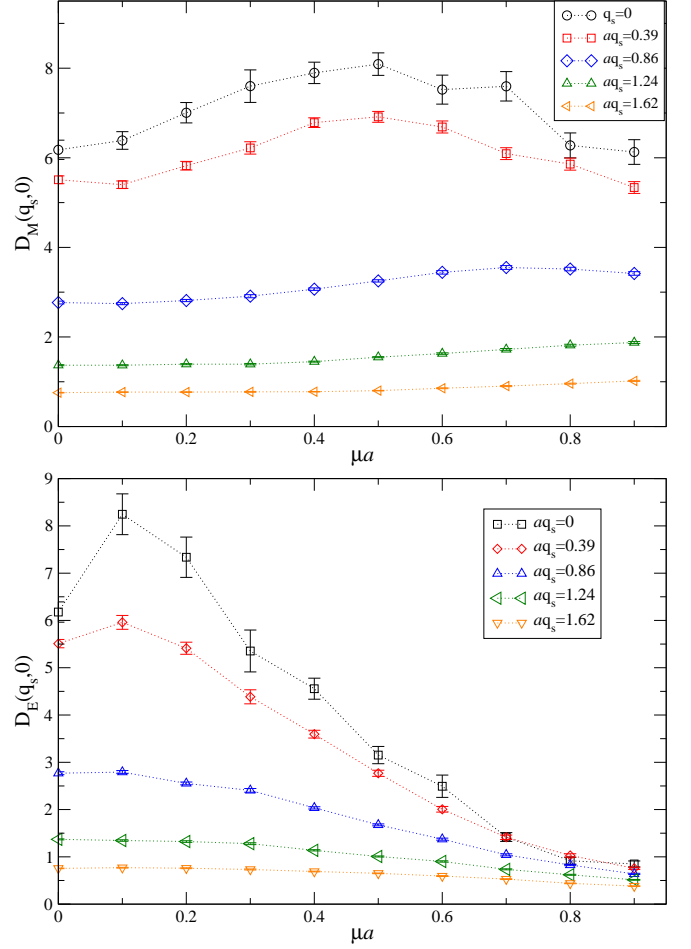


**Fig. 7.** The zero Matsubara mode of the magnetic (top) and electric (bottom) gluon propagator as a function of chemical potential  $\mu$  for selected values of the spatial momentum  $q_s$ , for the  $16^3 \times 8$  lattice.

First, in figure 5 we show the gluon propagator and dressing function in the vacuum for our two volumes,  $12^3 \times 24$  and  $16^3 \times 24$ . Comparing the data for the two volumes, we see that finite volume effects are modest for these lattices. In order to reduce ultraviolet lattice artefacts, we have applied a weak cylinder cut [34]. The propagator exhibits the usual infrared suppression observed in other lattice studies.

In figure 6 we show the two lowest Matsubara modes for selected spatial momenta as a function of chemical potential from the  $N_\tau = 24$  lattices for different spatial volumes. We find at most a very mild volume dependence, even for zero spatial momentum, with some indication that the magnetic propagator is slightly smaller on the larger volume. Note that because the available (discrete) momentum values depend on the spatial volume, the selected momenta from the  $12^3$  and  $16^3$  lattices do not match precisely, and the discrepancy between the propagator values on the two lattices at nonzero spatial momentum  $q_s = |\mathbf{q}|$  is likely to be at least as much due to the slightly different values of  $q_s$  as to finite volume effects.



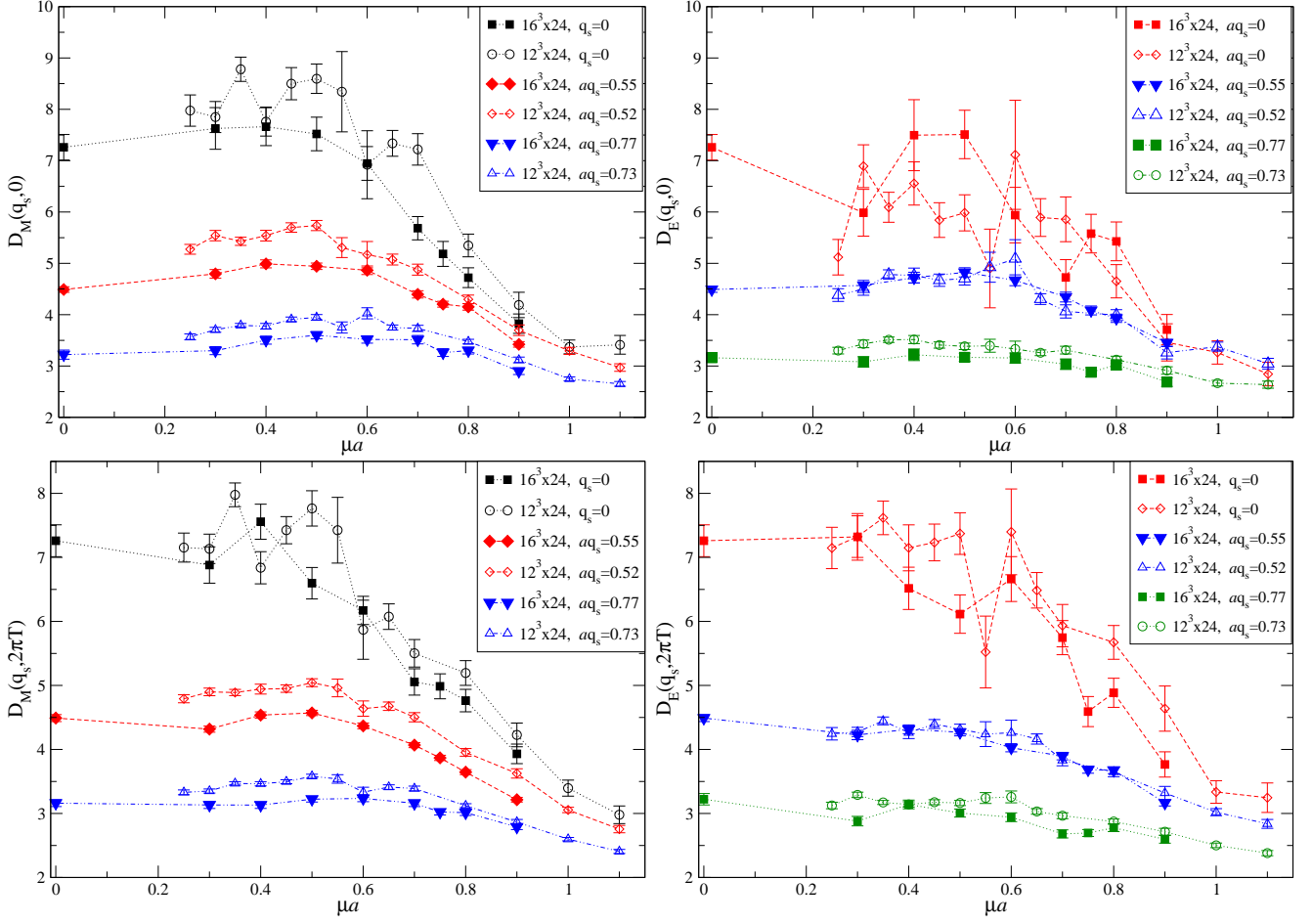


**Fig. 6.** The zeroth (top) and first (bottom) Matsubara mode of the magnetic (left) and electric (right) gluon propagator as a function of chemical potential  $\mu$  for selected values of the spatial momentum  $q_s$ , for  $N_\tau = 24$ , different spatial volumes.

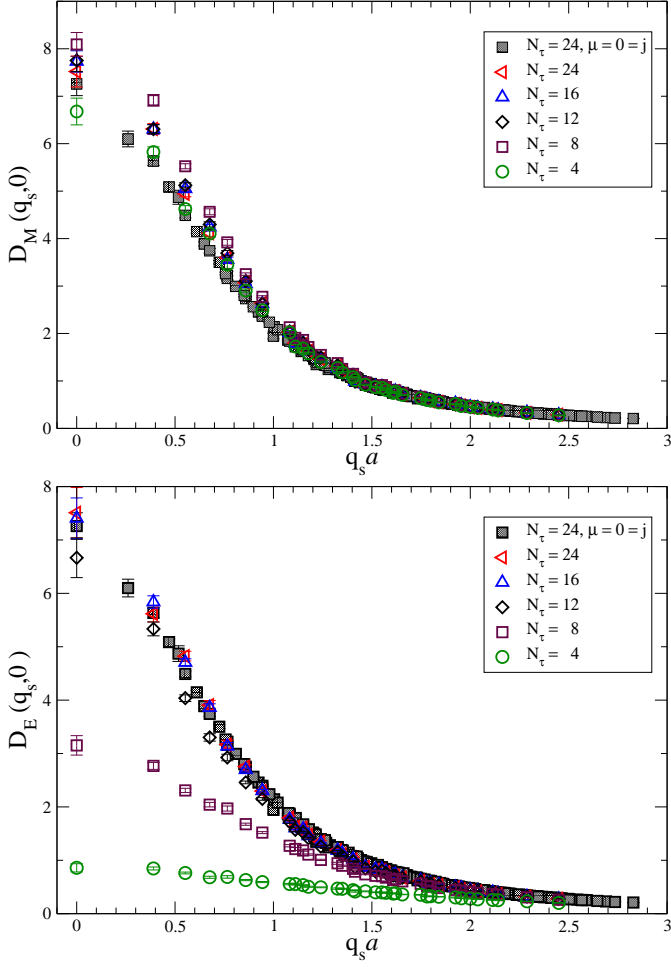
With respect to the infrared suppressed vacuum propagator shown in fig. 5 we find a mild enhancement at intermediate  $\mu$ , i.e. in the superfluid, confined phase, but a suppression in the deconfined phase, i.e. for large  $\mu$  for both tensor structures.

Figure 7 shows the lowest Matsubara mode for the high-temperature,  $16^3 \times 8$  lattice, again as a function of chemical potential and for several different spatial momenta. Here we find a considerably more complex picture. The electric form factor becomes progressively more suppressed with increasing  $\mu$  for all momenta, while for the magnetic form factor the lowest momentum modes show an interesting behaviour, with a peak at  $\mu a \approx 0.5$ . For large spatial momenta this form factor is instead enhanced at large  $\mu$ .

We now turn to the thermal behaviour of the gluon propagator at fixed chemical potential. Fig. 8 shows the zeroth Matsubara modes of the propagators for  $\mu a = 0.5$  and  $ja = 0.04$  on a spatial  $16^3$  lattice as a function of temperature, with higher modes shown in fig. 9. The magnetic component is slightly enhanced by the effect of chemical potential with respect to the vacuum, but interestingly it hardly feels thermal effects over a large range of low to intermediate temperatures, above which it becomes

screened. The electric propagator is suppressed for lower temperatures already. In pure gauge theory [35, 36, 37, 38, 39, 40, 41] the zero mode of the electric gluon shows strong enhancement for temperatures below the deconfinement transition, whereas the magnetic gluon is screened also below that transition. However fig. 2 entails that the chosen value of  $\mu$  drives the system close to the phase transition already at  $N_\tau = 20$ , and hence electric gluon enhancement may not be observed here. The interplay of temperature with chemical potential may also trigger the observed non-suppression for the magnetic mode. Our results are however in qualitative agreement with those obtained in a recent study of QCD with twisted-mass fermions [42]. A more detailed analysis of both medium effects and in particular their mutual interaction will be presented elsewhere.

To further quantify the variation of the gluon propagator with  $T$  and  $\mu$  we employ a global fit  $D_{M/E}^{\text{fit}}(q^2)$  to all modes, with  $q^2 = \mathbf{q}^2 + q_0^2$ . The functional form we use is inspired by [36]. However, for the momenta at hand the perturbative running of [36] can be neglected. In the



**Fig. 8.** Thermal behaviour of the zeroth Matsubara mode of the magnetic (top) and electric (bottom) propagators at  $\mu a = 0.5$  and  $ja = 0.04$  on  $16^3 \times N_\tau$  lattices.

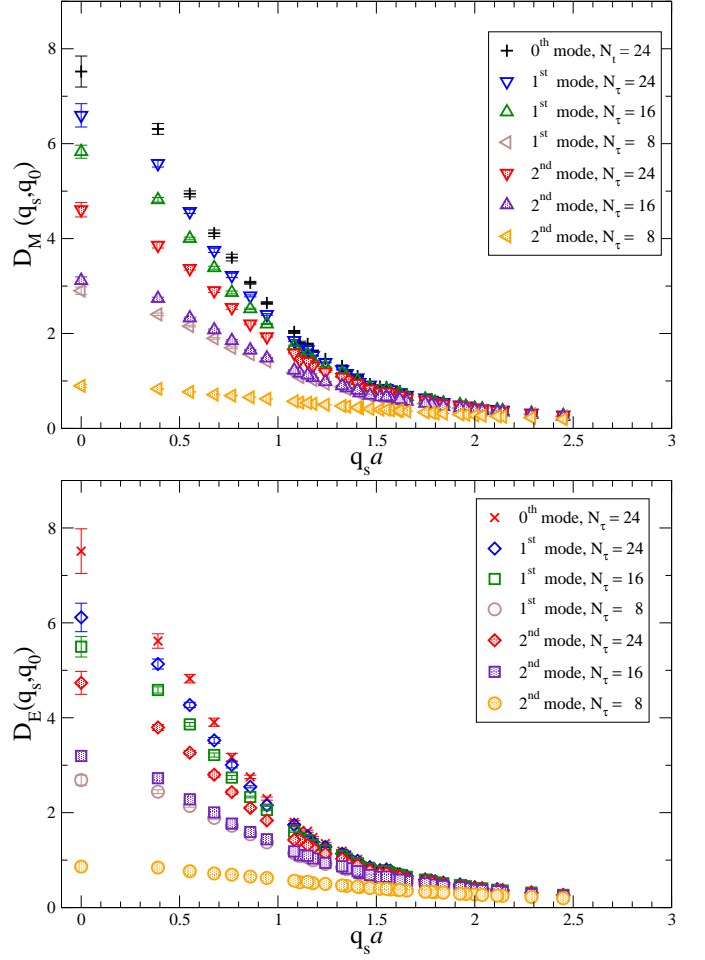


**Fig. 9.** Thermal behaviour of higher Matsubara modes of the magnetic (top) and electric (bottom) gluon propagators.

vacuum this gives us a three-parameter fit

$$D_{M/E}^{\text{fit}}(q^2) = \frac{\Lambda^2}{(q^2 + \Lambda^2)^2} (q^2 + \Lambda^2 a_{M/E})^{-b_{M/E}}. \quad (10)$$

At  $\mu = 0 = j$  we find  $\Lambda a = 0.999(3)$ ,  $a_M = a_E = 6.85(3)$  and  $b_M = b_E = -1.031(2)$  on the  $16^3 \times 24$  lattice, with a  $\chi^2$  per degree of freedom of around 8 for the magnetic mode and 5 for the electric mode. There is a slight volume dependence, with the  $12^3 \times 24$  lattice yielding  $\Lambda = 0.961(5)$ . The normalisation  $\Lambda$  is taken to be independent of  $T$  and  $\mu$ , but medium effects modify  $a_{M/E}$  and  $b_{M/E}$  for magnetic and electric modes individually. The results for the fit parameters are shown in fig. 10 as functions of  $N_\tau$  on the  $16^3 \times N_\tau$  lattices at  $\mu a = 0.5$  and  $ja = 0.04$ , and in fig. 11 as functions of  $\mu$  and lattice volume. For the available data we have found the dependence on  $j$  to be weak. At  $N_\tau = 5$  we did not obtain any satisfactory fit for the magnetic form factor, so these points are absent from fig. 10.

To illustrate the quality of these fits, fig. 12 shows the fits for  $\mu a = 0.5$ ,  $ja = 0.04$  on the  $16^3 \times 24$  lattice. We see that (10) gives a reasonable description for both modes,

but the underlying Ansatz that the gluon propagator is a function of the four-momentum  $q^2$  only, works less well for the magnetic form factor. The  $\chi^2/N_{df}$  is around 10 for most fits, with the electric form factor giving in general a somewhat better  $\chi^2$ . We are also planning to employ fit models inspired by hard dense loop perturbation theory, which depends separately on  $q_s$  and  $q_0$ .

## 6 Conclusions

We have carried out a detailed investigation of several aspects of 2-colour, 2-flavour QCD with  $m_\pi/m_\rho \approx 0.8$  at nonzero temperature  $T$  and quark chemical potential  $\mu$ . Our main findings are summarised below.

1. We have located the superfluid to normal and deconfinement transitions in the region  $0.35 \leq \mu a \leq 0.6$  ( $\mu = 385 - 665$  MeV). The superfluid to normal transition temperature  $T_s$  is remarkably constant in this region, while the deconfinement temperature  $T_d$  shows a decrease with  $\mu$  which appears to continuously connect to the  $\mu = 0$  transition identified in [7]. It also



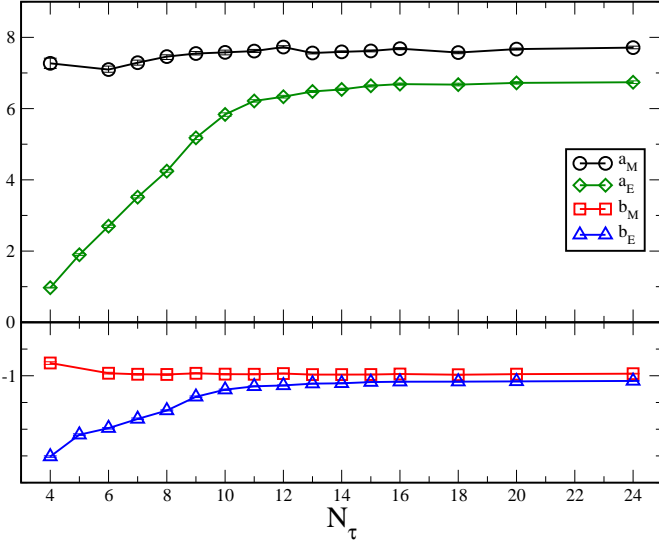


**Fig. 10.**  $N_\tau$  dependence of fit parameters  $a_{M/E}$  and  $b_{M/E}$  for  $16^3 \times N_\tau$  lattices at  $\mu a = 0.5$  and  $j a = 0.04$ .

appears to extrapolate smoothly to the high- $\mu$ , low- $T$  transition previously observed [5,6,7], although in the absence on any accurate data for the Polyakov loop at low temperature this must be taken merely as indicative.

2. The superfluid to normal transition appears to behave like a second order phase transition, while the deconfinement transition looks like a smooth crossover. This would have to be backed up with a careful finite volume and critical scaling analysis.
3. The static quark potential at low temperature appears to become more, rather than less confining at large  $\mu$ , suggesting that the dense medium with  $\langle L \rangle \neq 0$  is not an ordinary, deconfined quark-gluon plasma. It must however be noted that string breaking will occur even though it is not seen in the potential obtained from the Wilson loop because of the poor overlap with the relevant states.
4. The electric (longitudinal) gluon propagator in Landau gauge becomes strongly screened with increasing temperature and chemical potential. The magnetic (transverse) gluon shows little sensitivity to temperature, and exhibits a mild enhancement at intermediate  $\mu$  before coming suppressed at large  $\mu$ .

The structure of the phase diagram is summarised in fig. 13. We also include the estimates for the deconfinement transition given in [7]. We see that these are consistent with, but slightly above, our new estimates in this paper. The indications are that the deconfinement line crosses the superfluid to normal transition line, giving rise to a region of deconfined, superfluid matter, but in the absence of precise data at larger  $\mu$ , we can not say this with any degree of certainty. To map out the phase boundaries with greater precision and to clearly establish the order of the transitions, large-scale simulations on several spatial volumes will be required. This goes beyond our current

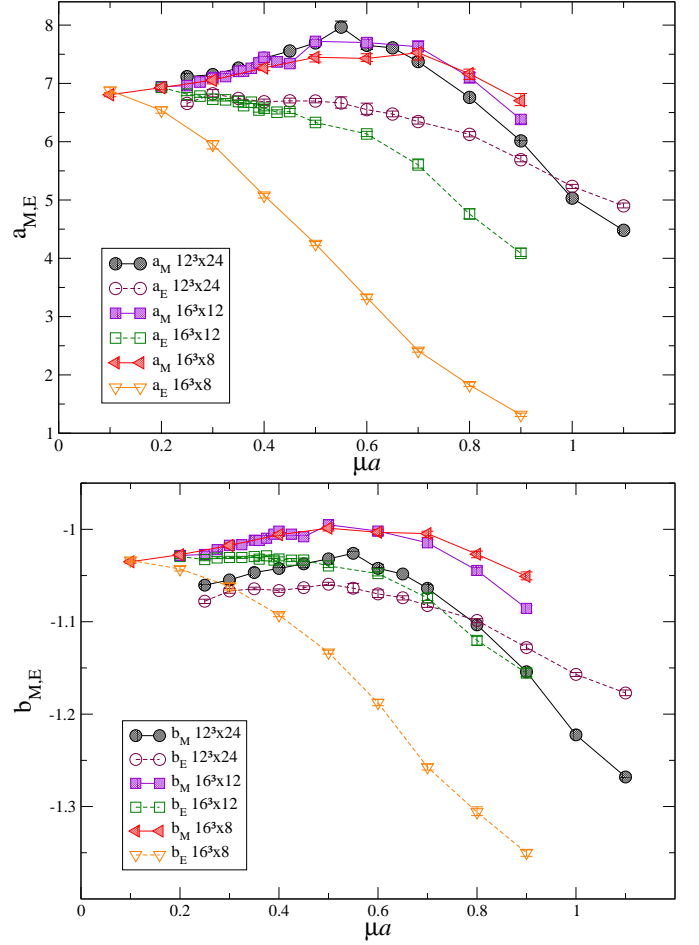


**Fig. 11.** Dependence of fit parameters  $a_{M/E}$  (top) and  $b_{M/E}$  (bottom) on  $\mu$  and lattice volume.

computational capabilities, but is an interesting topic for future investigations.

The lack of screening (and even antiscreening) observed in the static quark potential requires further investigation to establish whether this is a signal of an exotic state of matter or a result of poor overlap with relevant states and/or lattice artefacts. We are planning to compute the static quark potential at higher temperatures, using both the Wilson loop and Polyakov loop correlator, to further elucidate this.

The screening of the static magnetic gluon propagator (zero Matsubara mode) at high  $\mu$  and low  $T$  is a clear signal of the breakdown of resummed perturbation theory, which predicts that this mode is unscreened to all orders. This is likely to be relevant also for real QCD, and should be taken into account in any future study using model gluon propagators to compute for example the superfluid or superconducting gap.

In an ongoing study we will compare the lattice gluon propagator at non-vanishing chemical potential and temperature with results from functional continuum methods, extending studies of thermal propagators [43,44,45] to finite density. As there are no insurmountable problems in

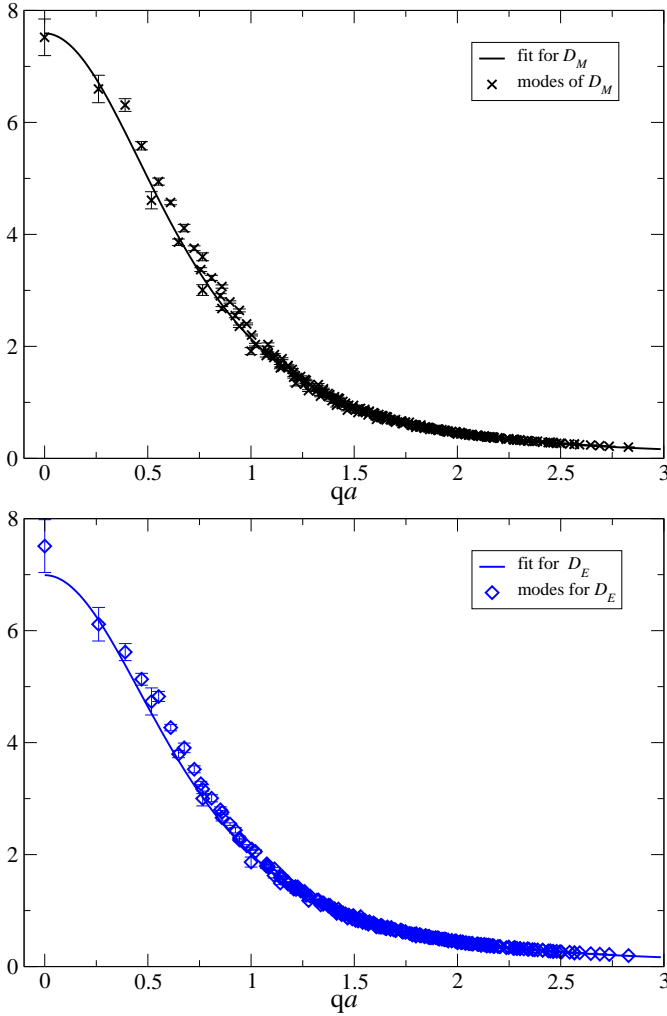


**Fig. 12.** Multimodal fits of the form eq. (10) for the magnetic (top) and electric (bottom) gluon propagators at  $a\mu = 0.5$  and  $aj = 0.04$  on the  $16^3 \times 24$  lattice. Note that the functions are plotted versus four-momentum  $q$  on the abscissa.

QC<sub>2</sub>D, in particular no sign problem, a direct analysis serves to identify possible technical limitations in either method, stemming from finite size and finite volume artefacts in the lattice formulation, or from inevitably necessary truncations in the continuum description. We are also in the process of computing the quark propagator, which will give further input to these studies.

We are currently extending our study of QC<sub>2</sub>D to smaller lattice spacings, which will enable us to perform a controlled extrapolation to the continuum limit and clarify the possible role of lattice artefacts at large  $\mu$ .

This work is carried out as part of the UKQCD collaboration and the DiRAC Facility jointly funded by STFC, the Large Facilities Capital Fund of BIS and Swansea University. We thank the DEISA Consortium ([www.deisa.eu](http://www.deisa.eu)), funded through the EU FP7 project RI-222919, for support within the DEISA Extreme Computing Initiative. The simulation code was adapted with the help of Edinburgh Parallel Computing Centre funded

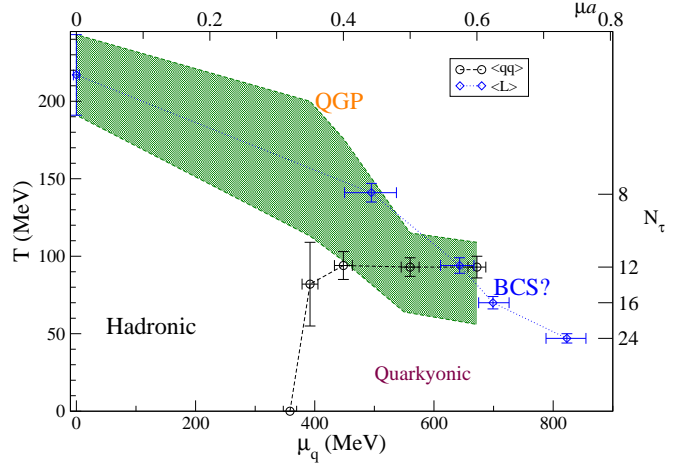


**Fig. 13.** Phase diagram of QC<sub>2</sub>D with  $m_\pi/m_\rho = 0.8$ . The black circles denote the superfluid to normal phase transition; the green band the deconfinement crossover. The blue diamonds are the estimates for the deconfinement line from [7].

by a Software Development Grant from EPSRC. We acknowledge the use of the USQCD cluster at Fermilab for part of this work. The work has been carried out with the support of Science Foundation Ireland grant 11-RFP.1-PHY3193. DM is supported by U.S. Department of Energy grant under contract no. DE-FG02-85ER40237. We thank Pietro Giudice, Simon Hands and Jan Pawłowski for stimulating discussions and advice.

## References

1. G. Aarts, F. A. James, E. Seiler and I.-O. Stamatescu, *Eur.Phys.J.* **C71**, 1756 (2011), [arXiv:1101.3270].
2. G. Aarts, PoS **LATTICE2012**, 017 (2012), [arXiv:1302.3028].
3. S. Chandrasekharan, *Phys.Rev.* **D86**, 021701 (2012), [arXiv:1205.0084].
4. AuroraScience Collaboration, M. Cristoforetti, F. Di Renzo and L. Scorzato, *Phys.Rev.* **D86**, 074506 (2012), [arXiv:1205.3996].
5. S. Hands, S. Kim and J.-I. Skullerud, *Eur. Phys. J.* **C48**, 193 (2006), [hep-lat/0604004].
6. S. Hands, S. Kim and J.-I. Skullerud, *Phys. Rev.* **D81**, 091502R (2010), [arXiv:1001.1682].
7. S. Cotter, P. Giudice, S. Hands and J.-I. Skullerud, *Phys.Rev.* **D87**, 034507 (2013), [arXiv:1210.4496].
8. A. Maas, L. von Smekal, B. Wellegehausen and A. Wipf, arXiv:1203.5653.
9. J. B. Kogut and D. K. Sinclair, *Phys. Rev.* **D66**, 034505 (2002), [hep-lat/0202028].
10. S. Hands *et al.*, *Eur. Phys. J.* **C17**, 285 (2000), [hep-lat/0006018].
11. P. Cea, L. Cosmai, M. D'Elia and A. Papa, *JHEP* **0702**, 066 (2007), [arXiv:hep-lat/0612018].
12. P. Cea, L. Cosmai, M. D'Elia, C. Manneschi and A. Papa, *Phys.Rev.* **D80**, 034501 (2009), [arXiv:0905.1292].
13. T. Brauner, K. Fukushima and Y. Hidaka, *Phys. Rev.* **D80**, 074035 (2009), [arXiv:0907.4905].

14. J. O. Andersen and T. Brauner, Phys. Rev. **D81**, 096004 (2010), [arXiv:1001.5168].
15. N. Strodthoff, B.-J. Schaefer and L. von Smekal, Phys.Rev. **D85**, 074007 (2012), [arXiv:1112.5401].
16. J. Braun, H. Gies and J. M. Pawłowski, Phys.Lett. **B684**, 262 (2010), [arXiv:0708.2413].
17. F. Marhauser and J. M. Pawłowski, arXiv:0812.1144.
18. J. Braun, A. Eichhorn, H. Gies and J. M. Pawłowski, Eur.Phys.J. **C70**, 689 (2010), [arXiv:1007.2619].
19. L. Fister and J. M. Pawłowski, arXiv:1301.4163.
20. J.-I. Skullerud, Nucl. Phys. **A820**, 175c (2009), [arXiv:0810.3795].
21. J.-I. Skullerud, PoS **QCD-TNT09**, 043 (2009), [arXiv:0912.0844].
22. S. Cotter *et al.*, PoS **LATTICE2012**, 091 (2012), [arXiv:1210.6757].
23. S. Borsányi *et al.*, Phys.Lett. **B713**, 342 (2012), [arXiv:1204.4089].
24. K. G. Wilson, Phys.Rev. **D10**, 2445 (1974).
25. M. Laine, O. Philipsen, P. Romatschke and M. Tassler, JHEP **0703**, 054 (2007), [arXiv:hep-ph/0611300].
26. N. Brambilla, J. Ghiglieri, A. Vairo and P. Petreczky, Phys.Rev. **D78**, 014017 (2008), [arXiv:0804.0993].
27. A. Beraudo, J.-P. Blaizot and C. Ratti, Nucl.Phys. **A806**, 312 (2008), [arXiv:0712.4394].
28. A. Beraudo, J. Blaizot, P. Faccioli and G. Garberoglio, Nucl.Phys. **A846**, 104 (2010), [arXiv:1005.1245].
29. A. Bazavov and P. Petreczky, arXiv:1210.6314.
30. T. Kawanai and S. Sasaki, Phys.Rev. **D85**, 091503 (2012), [arXiv:1110.0888].
31. C. Allton, W. Evans and J.-I. Skullerud, PoS **LATTICE2012**, 082 (2012).
32. S. Hands, S. Kim and J.-I. Skullerud, Phys.Lett. **B711**, 199 (2012), [arXiv:1202.4353].
33. SESAM Collaboration, G. S. Bali, H. Neff, T. Düssel, T. Lippert and K. Schilling, Phys.Rev. **D71**, 114513 (2005), [arXiv:hep-lat/0505012].
34. UKQCD, D. B. Leinweber, J. I. Skullerud, A. G. Williams and C. Parrinello, Phys. Rev. **D60**, 094507 (1999), [hep-lat/9811027].
35. A. Cucchieri, A. Maas and T. Mendes, Phys.Rev. **D75**, 076003 (2007), [arXiv:hep-lat/0702022].
36. C. S. Fischer, A. Maas and J. A. Muller, Eur. Phys. J. **C68**, 165 (2010), [arXiv:1003.1960].
37. V. Bornyakov and V. Mitrjushkin, Int.J.Mod.Phys. **A27**, 1250050 (2012), [arXiv:1103.0442].
38. A. Maas, Phys. Rep. in press (2013), [1106.3942].
39. R. Aouane *et al.*, Phys.Rev. **D85**, 034501 (2012), [arXiv:1108.1735].
40. A. Maas, J. M. Pawłowski, L. von Smekal and D. Spielmann, Phys.Rev. **D85**, 034037 (2012), [arXiv:1110.6340].
41. A. Cucchieri and T. Mendes, PoS **FACESQCD**, 007 (2010), [arXiv:1105.0176].
42. R. Aouane, F. Burger, E.-M. Ilgenfritz, M. Muller-Preussker and A. Sternbeck, arXiv:1212.1102.
43. L. Fister and J. M. Pawłowski, arXiv:1112.5440.
44. L. Fister and J. M. Pawłowski, arXiv:1112.5429.
45. L. Fister, PhD thesis, Heidelberg University (2012).